Optimizing Nanoparticle Designs for Ideal Absorption of Light

Victor Grigoriev, Nicolas Bonod, Jérôme Wenger, Brian Stout

Optimizing Nanoparticle Designs for Ideal Absorption of Light

Victor Grigoriev, Nicolas Bonod, Jérôme Wenger, and Brian Stout
CNRS, Aix-Marseille Université, Centrale Marseille, Institut Fresnel, UMR 7249, Campus de St. Jérôme, 13397 Marseille, France

Resonant interaction of light with nanoparticles is essential for a broad range of nanophotonics and plasmonics applications, including optical antennas, photovoltaics, thermoplasmonics, and sensing. Given this broad interest, analytical formulas are highly desirable to provide design guidelines for reaching the conditions of ideal absorption. Here we derive analytical expressions to accurately describe the electric and magnetic modes leading to ideal absorption. Our model significantly improves on accuracy as compared to classical models using Green's functions or a Mie coefficient expansion. We demonstrate its applicability over a broad parameter space of frequencies and particle diameters up to several wavelengths. We reveal that ideal absorption is attainable in homogeneous spherical nanoparticles made of gold or silver at specific sizes and illumination frequencies. To reach ideal absorption at virtually any frequency in the visible and near infrared range, we provide explicit guidelines to design core-shell nanoparticles. This work should prove useful for providing experimental designs that optimize absorption and for a better understanding of the physics of ideal absorption. **Keywords :** *Ideal absorption, Coherent Perfect Absorption, Plasmonics, Scattering theory, Mie theory, Optical magnetic modes, resonant photonics.*

Metallic nanoparticles, and more recently dielectric nanoparticles, are receiving tremendous attention due to their ability to concentrate light energy into volumes at the nanometer scale [1, 2]. Light-matter interaction around nanoparticles is at the core of a wide range applications including optical antennas,[3] light harvesting,[4] thermoplasmonics,[5] and local surface plasmon resonance sensing[6]. In this context, optimizing the design of nanoparticles to maximize absorption of light is of crucial importance.[7, 8] This will lead to enhanced light-matter interaction, photoluminescence or heat generation.

While brute force numerical simulations can certainly answer the question and provide reliable design parameters, they come at the price of extensive parameter searches and a lack of physical insight. Analytical expressions for simple and faultless nanoparticle geometries are therefore interesting as they are quite straightforward for other researchers to use and provide insights into light absorption problems. However, as we will show below, classical point-like dipole models are inaccurate for nanoparticles of sizes $\gtrsim$ 30nm, and a more realistic model needed to to be developed.

In this manuscript, we develop a conceptual framework to achieve ideal absorption of light by metallic and dielectric nanoparticles over a broad parameter space of frequencies and particle sizes. We define Ideal Absorption (IA) as the conditions leading to a mode of the total field being completely absorbed by the nanoparticle. Ideal absorption is also sometimes referred to as "coherent perfect absorption"[9–11]. However, it should be pointed out that absorption of the incident field is only perfect for an ideal 4π illumination specifically tailored to the IA mode.[12]

As our main result, eq.(16) provides explicitly analytical formulas describing the conditions to reach IA for homogeneous spherical nanoparticles. For such particles, only a restricted number of attainable parameters (radius, permittivity, frequency) reach ideal absorption. We proceed to show that core-shell nanoparticles feature the ability to satisfy the ideal light absorption condition over the full visible spectrum by tuning the filling factor and the radius of the nanoparticle. We provide explicit guidelines (eq. (18)) to optimize the design so as to reach ideal absorption for silver and gold core-shell nanoparticles.

The manuscript is organized as follows: in Section 1, we introduce ideal absorption and demonstrate that it corresponds to a fundamental upper bound in an absorption cross section channel ($\sigma_{\rm a} = 3\lambda^2/8\pi$ for dipole resonators). We then discuss in Section 2 two classical 'point-like' models providing analytical formulas for predicting fundamental electric dipole IA (eq. (12)). Since these models are limited to treatments of fundamental electric modes and make rather inaccurate predictions for all but the smallest particle sizes, we derive significantly improved analytic formulas in Eq.(16) predicting the required electric and magnetic fundamental dipole IA solutions in homogeneous scatterers. Section 3 shows numerical results using a Weierstrass factorization method [13, 14] that determines fundamental and higher order IA modes to arbitrary accuracy. After some discussion and calculations concerning multi-mode absorption and IA bandwidth, Section 4 illustrates some predictions for IA in homogeneous spheres with gold and silver at specific frequencies and sizes. Finally, the discussion is extended to core-shell nanoparticles (Section 5). Combining eq. (18) with eq. (16a), we provide a simple procedure to design optimized core-shells achieving IA at essentially any frequency in the visible and near visible range.

I. SCATTERING THEORY FOR IDEAL ABSORPTION

Scattering in three dimensional electromagnetic problems is conveniently expressed in terms of incoming and outgoing spherical Vector Partial Waves (VPWs).[15]

The VPWs are solutions of homogeneous media Maxwell equations of either electric source type ($e:\ {}^{(\pm)}_{n,m}(k\mathbf{r})$) or magnetic source type ($h:\ M^{(\pm)}_{n,m}(k\mathbf{r})$), with the $+(-)$ superscripts indicating that the functions satisfy outgoing (incoming) boundary conditions respectively. The subscript, n, denotes the total angular momentum number, and $m=-n,...,n$, the angular momentum projection number.[15] The spatial dependence of the VPWs is scaled by the in-medium wavenumber, $k=\sqrt{\varepsilon_b\mu_b}\omega/c = N_b\omega/c = 2\pi/\lambda$, where N_b is the refraction index of the homogeneous background material, and λ, the in-medium wavelength.

Theoretical treatments of electromagnetic scattering from a homogeneous spherically symmetric particle go under the names of Lorenz-Mie-Debye theory, but the physical content is best viewed in the formalism of S or T matrices, originally developed for quantum mechanical scattering theory.[15–19, 22] The S-matrix seems best adapted to the discussion of IA, and is privileged from here on.

The *total field* in a homogeneous region surrounding a particle can always be developed on the basis set of the incoming and outgoing VPWs, with $a^{(e,\pm)}_{n,m}$ and $a^{(h,\pm)}_{n,m}$ respectively denoting the electric and magnetic mode VPWs field coefficients. Since the S-matrix of a spherically symmetric system is automatically diagonal in the VPW basis, its elements express the linear relationship between the outgoing and incoming field coefficients of the total field for both electric and magnetic source fields respectively, *i.e.* $S^{(e)}_n = a^{(e,+)}_{n,m}/a^{(e,-)}_{n,m}$, and $S^{(h)}_n = a^{(h,+)}_{n,m}/a^{(h,-)}_{n,m}$.

Algebraic manipulations involving the T-matrix[15, 16], and the definition of the S-matrix[15, 18], $\overline{\overline{S}} \equiv \overline{\overline{I}} + 2\overline{\overline{T}}$, provide convenient expressions for the S-matrix coefficients:

$$S^{(e)}_n = -\frac{h^{(-)}_n(kR)}{h^{(+)}_n(kR)}\cdot\frac{\overline{\varepsilon}_s\varphi^{(-)}_n(kR)-\varphi_n(k_sR)}{\overline{\varepsilon}_s\varphi^{(+)}_n(kR)-\varphi_n(k_sR)} \tag{1a}$$

$$S^{(h)}_n = -\frac{h^{(-)}_n(kR)}{h^{(+)}_n(kR)}\cdot\frac{\overline{\mu}_s\varphi^{(-)}_n(kR)-\varphi_n(k_sR)}{\overline{\mu}_s\varphi^{(+)}_n(kR)-\varphi_n(k_sR)}\ , \tag{1b}$$

where, $\overline{\varepsilon}_s \equiv \varepsilon_s/\varepsilon_b$, and $\overline{\mu}_s \equiv \mu_s/\mu_b$ are respectively the permittivity and permeability contrasts between the sphere and the host medium, and k_s is the wavenumber inside the sphere. The $h^{(+)}_n(x)$ and $h^{(-)}_n(x)$ functions respectively denote the outgoing and incoming spherical Hankel functions. The expressions in eq.(1) also employ the functions:

$$\varphi^{(\pm)}_n(x) \equiv \frac{\left[xh^{(\pm)}_n(x)\right]'}{h^{(\pm)}_n(x)}\ , \qquad \varphi_n(x) \equiv \frac{[xj_n(x)]'}{j_n(x)}\ , \tag{2}$$

where $j_n(x)$ are the nth order spherical Bessel functions.

Flux conservation imposes an upper bound on the amplitude of the S matrix elements, $\left|S^{(e,h)}_n\right| \leq 1$, where the upper limit, $\left|S^{(e,h)}_n\right| = 1$ is satisfied by any lossless scatterer since this condition results directly in $\left|a^{(+)}_{n,m}\right| = \left|a^{(-)}_{n,m}\right|$.[18] The S-matrix of a lossless scatterer is characterized by zeros (absorbing modes) in the upper-half complex frequency plane, and poles (emitting modes) in the lower-half plane frequency plane.[13, 14] Adding absorption to the particle causes the absorbing modes to descend towards (and finally into) the lower complex plane with IA occurring at those values of $\overline{\varepsilon}_s$ for which a zero of the S-matrix lies on the real frequency axis, *i.e.* there exists an n such that:

$$S^{(e)}_n = 0 \Leftrightarrow \frac{\varphi_n(k_sR)}{\overline{\varepsilon}_s} = \varphi^{(-)}_n(kR)\ ,\ \text{or}\ , \tag{3a}$$

$$S^{(h)}_n = 0 \Leftrightarrow \frac{\varphi_n(k_sR)}{\overline{\mu}_s} = \varphi^{(-)}_n(kR)\ , \tag{3b}$$

when $\Im\{\omega\} = 0$ (these conditions being found by inspection of eq. (1a) and eq. (1b).

Scattering and absorption cross sections of a spherically symmetric scatterer are the sum of the contributions from all multi-pole orders, n:

$$\sigma_{\rm s} = \sum_{n=1}^{\infty}\left(\sigma^{(e)}_{n,{\rm s}} + \sigma^{(h)}_{n,{\rm s}}\right)\ , \quad \sigma_{\rm a} = \sum_{n=1}^{\infty}\left(\sigma^{(e)}_{n,{\rm a}} + \sigma^{(h)}_{n,{\rm a}}\right)\ . \tag{4}$$

The multi-pole contributions to the extinction, scattering, and absorption cross sections[15, 18, 19] can be respectively expressed in terms of the S-matrix as:

$$\sigma^{(e,h)}_{n,{\rm a}} = \frac{\pi}{2k^2}(2n+1)\left(1-\left|S^{(e,h)}_n\right|^2\right) \tag{5a}$$

$$\sigma^{(e,h)}_{n,{\rm s}} = \frac{\pi}{2k^2}(2n+1)\left|S^{(e,h)}_n - 1\right|^2 \tag{5b}$$

$$\sigma^{(e,h)}_{n,{\rm e}} = \frac{\pi}{k^2}(2n+1)\,\Re\left\{1-S^{(e,h)}_n\right\}\ , \tag{5c}$$

where the $2n+1$ factors arise from the azimuthal mode degeneracy of the orbital modes.

One finds that an IA mode contributes equally to the absorption and scattering cross sections by inserting the IA criteria, $S_n = 0$ into eq. (5a) and eq. (5b) (in either the (e) or (h) channels), with values of:[20, 21]

$$\sigma_{n,{\rm s}} = \sigma_{n,{\rm a}} = \frac{2n+1}{8\pi}\lambda^2\ , \tag{6}$$

which is an upper bound for the absorption cross section of a mode, but a factor four times less than the $S_n = -1$, *unitary limit*[17] of the scattering or extinction cross sections, obtainable from eq. (5b) and eq. (5c). The equality of scattering and absorption cross sections in an IA channel follows from the fact that IA requires the field scattered by the particle to have perfectly destructive interference with the outgoing wave components of the local excitation field (leaving the nth order modes of the total field to be purely incoming). We also remark that many properties of IA in particles, like eq. (6), find

analogues in the ideal absorption of 1D systems, where for example the maximum absorption coefficient, A, of a plane wave illuminating a single side of a symmetric thin film occurs when $A = R + T = 0.5$.[23, 24]

Since the $\varphi_n^{(-)}(kR)$ is a complex function of a real variable, and $\varphi_n(k_s R)$ is real for real valued k_s, the IA solutions of eq. (3a) or eq. (3b) can occur only for complex values of $\overline{\varepsilon}_s$. Furthermore, eqs.(3) are transcendental equations, and each has an infinite number of solutions. For the sake of clarity, further discussion in this work will be limited to the $n = 1$ (*i.e.* dipole) mode solutions of eq.(3).

The real and imaginary parts of the solutions of eq. (3a) with the lowest values of $\Re\{\overline{\varepsilon}_s\}$ are plotted as the blue(solid) line in fig. 1 for particle diameters ranging from zero up to a little more than a wavelength. These results were computed by taking advantage of the newly developed Weierstrass factorization for resonant photonic structures.[13, 14] One readily remarks that this solution tends to the well-known quasi-static dipolar plasmon resonance at $\overline{\varepsilon}_s = -2$ when $kR \to 0$. When only this IA mode is of interest, one can try to describe IA with a 'point-like' model aimed at providing approximate descriptions of the lowest $\Re\{\overline{\varepsilon}_s\}$ electric dipole resonance[25, 26]. This is the aim of the next section.

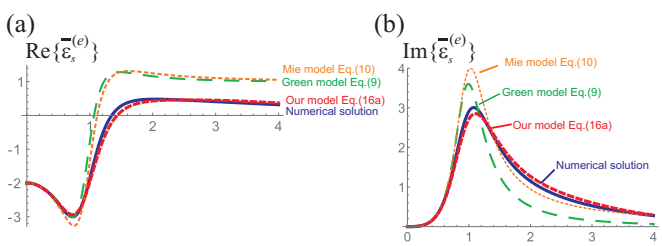

FIG. 1. Numerical results of the real and imaginary parts of $\overline{\varepsilon}_s$ yielding the lowest IA solution are plotted as a function of kR (blue solid curves). The predictions from the Green function point-like model eq. (9) are plotted in green (long dashed lines), and the Mie theory development model eq. (10) are plotted in orange (dotted lines). Our analytical model eq. (16a) (red short dashed curves) provides an improved description of the conditions to reach Ideal Absorption over a broad kR range.

II. POINT-LIKE MODELS AND ANALYTIC EXTENSIONS

Unitarity considerations[15, 17, 18] dictate that the polarizability of a small isotropic scatterer takes the form:[27–29]

$$\alpha_e^{-1} = \alpha_{\rm qs}^{-1} - i\frac{k^3}{6\pi} \ , \tag{7}$$

where the quasi-static polarizability, $\alpha_{\rm qs}$, is real in the absence of absorption, while the $-ik^3/6\pi$ term accounts for radiative losses. Unitarity however does not dictate the finite frequency corrections to $\alpha_{\rm qs}$, and one only knows that $\alpha_{\rm qs}$ must tend towards its quasi-static value in the small kR limit:

$$\lim_{kR\to 0} \alpha_{\rm qs} = 4\pi R^3 \frac{\overline{\varepsilon}_s - 1}{\overline{\varepsilon}_s + 2} \equiv \alpha_0 \ , \tag{8}$$

where α_0 is the 'static' polarizability of a sphere. Some authors simply impose $\alpha_{\rm qs} = \alpha_0$, while others, using first principles Green's function theory and 'regularizations' of the point-like integrals, commonly derive a k^2 order correction to $\alpha_{\rm qs}^{-1}$ of the form:[26, 30, 31] :

$$\left[\alpha_{\rm qs}^{\rm (G.f)}\right]^{-1} \simeq \alpha_0^{-1} - \frac{k^2}{6\pi R} \ . \tag{9}$$

An alternative approach is to expand the exact Mie formula to lowest order in k^2, as proposed earlier by Moroz[27] (see also Stratton[32]), which leads to :

$$\left[\alpha_{\rm qs}^{\rm (M.t)}\right]^{-1} \simeq \alpha_0^{-1} - \frac{3}{5}\frac{\overline{\varepsilon}_s - 2}{\overline{\varepsilon}_s - 1}\frac{k^2}{4\pi R} \ . \tag{10}$$

It is a bit surprising that the factors multiplying the k^2 corrections of eq. (9) and eq. (10) do not agree. We relate this to the lack of rigor in the regularizations of the Green function derivation. It seems nevertheless desirable to include k^2 corrections to the polarizability since such corrections predict the physically observed 'red-shift' of localized plasmon resonances with increasing particle size.

Neither eq. (9) nor eq. (10) are strictly necessary for isotropic scatterers, since in this case the polarizability is directly related to the electric dipole S-matrix element, $S_1^{(e)}$, via the relation:[33]

$$\alpha_e = \frac{3\pi i}{k^3}\left(1 - S_1^{(e)}\right) \ , \tag{11}$$

thus predicting an IA polarizability of $\alpha_{\rm IA} = 3\pi i/k^3$. The advantage of adopting a point-like model is that if one replaces the left hand side of either eq. (9) or eq. (10) with $\alpha_{\rm IA}$, then one can algebraically solve for the value of $\overline{\varepsilon}_{\rm IA}^{(e)}$ as a function of the size parameter, $\rho \equiv kR$:

$$\overline{\varepsilon}_{\rm IA}^{(e)}(\rho) = \begin{cases} -2\frac{1+\frac{1}{3}\rho^2(1-i\rho)}{1-\frac{2}{3}\rho^2(1-i\rho)} & \text{Green function : eq. (9)} \\ \\ -2\frac{1+\frac{1}{15}\rho^2(9-5i\rho)}{1-\frac{1}{15}\rho^2(9+10i\rho)} & \text{Mie development : eq. (10)} \end{cases} \ . \tag{12}$$

The real and imaginary parts of these functions are plotted in fig. 1a, and fig. 1b. both point-like predictions for $\overline{\varepsilon}_{\rm IA}^{(e)}(kR)$ tend towards the exact result (blue curve) in the $kR \to 0$ limit, they differ significantly from the exact result and each other for larger kR.

In view of the inaccuracies of these traditional point-like models, we derive below more reliable predictions of the IA conditions by analyzing the pole structure of the special functions. One first remarks that the $\varphi_n^{(\pm)}$

functions appearing in eq. (1) have finite meromorphic expressions, which for the dipole example take the form:

$$h_1^{(\pm)}(z) = -e^{\pm iz}\frac{z \pm i}{z^2} \; ; \; \varphi_1^{(\pm)}(z) = \pm iz - \frac{1}{1 \mp iz} \; . \quad (13)$$

The φ_n functions on the other hand have an infinite number of poles located along the real axis, and can be expressed in meromorphic form as:

$$\varphi_n(z) = n + 1 + \sum_{\alpha=1}^{\infty}\left(\frac{2z^2}{z^2 - a_{n,\alpha}^2}\right) \; , \quad (14)$$

where the constants, $a_{n,\alpha}$, are the zeros of the spherical Bessel function, $j_n(x)$, and are tabulated.[34]

One can obtain analytic dipole approximations to eq. (1) by replacing φ_1 of eq. (14) with an approximate meromorphic function having the same two lowest poles, a and zeros, b:

$$\varphi_1(z) \approx 2\frac{1-(z/b)^2}{1-(z/a)^2} \; , \quad (15)$$

where $a = 1.4303\pi$ and $b = 0.87335\pi$. Adopting this substitution transforms $S_1^{(e,h)} = 0$ into quadratic equations in terms of $\overline{\varepsilon}_s^{(e,h)}$ whose relevant solutions are:

$$\overline{\varepsilon}_{\rm IA}^{(e)}(\rho) = \frac{1}{2}\frac{b^2}{\rho^2}\left[1 + \frac{\rho^2}{a^2}\frac{2(i\rho+1)}{(\rho^2 - i\rho - 1)} - \sqrt{\left(1 + \frac{\rho^2}{a^2}\frac{2(i\rho+1)}{(\rho^2 - i\rho - 1)}\right)^2 - \frac{\rho^2}{b^2}\frac{8(i\rho+1)}{(\rho^2 - i\rho - 1)}}\right] \quad (16a)$$

$$\overline{\varepsilon}_{\rm IA}^{(h)}(\rho) = \frac{3 + 3i\rho - \rho^2}{\rho^2\left(\frac{2+2i\rho}{b^2} + \frac{1+i\rho-\rho^2}{a^2}\right)} \; . \quad (16b)$$

This set of analytical formulas forms our first main result. It allows the accurate design of ideal absorbers in both electric and magnetic modes, and can be immediately used by other researchers to optimize absorption in nanoparticles. The electric dipole solution of eq. (16a) is plotted in red in fig. 1. It remarkably converges towards the numerical exact solution (blue curve) over a broad kR parameter range. The magnetic dipole solution of eq. (16b) is plotted in fig. 2c and fig. 2d, where it is visually indistinguishable from the numerically exact solution. Our new analytical formulas are thus valid up to particles sizes of several hundreds of nanometers, which constitutes an improvement of more than an order of magnitude in nanoparticle size with respect to classical 'point-like' models.

III. EXACT SOLUTIONS

Although the analytic expressions of Eq.(16) provide accurate approximations for the lowest IA modes, one may nevertheless desire higher precision or the predictions of additional IA solutions, either of which will require numerical solutions of eq. (3a) or eq. (3b). Finding these solutions is quite difficult when using commonly employed techniques involving Cauchy integrals in the complex plane or conjugate gradient methods; but they can be readily solved using techniques based on Weierstrass factorization[13, 14] which exploit the meromorphic expansion of eq. (14).

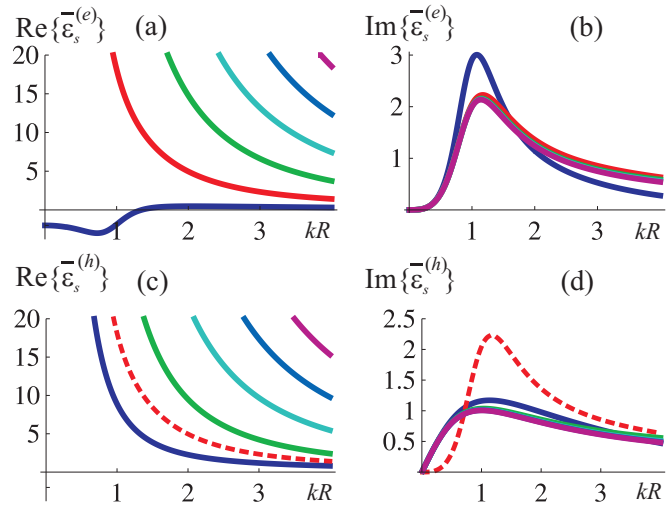

FIG. 2. Conditions to reach electric dipole Ideal Absorption as function of kR for the real (a) and imaginary (b) part of the complex permittivity $\overline{\varepsilon}_s$. Magnetic dipole IA values for $\overline{\varepsilon}_s$ are also plotted in (c,d). The lowest electric dipole solution with $\Re\{\overline{\varepsilon}_s\} > 1$ is plotted as a dashed curve in (c) and (d) for comparison.

The real and imaginary parts of the numerically obtained dipole solutions of eq. (3a) and eq. (3b) for the $\overline{\varepsilon}_s$ are plotted in fig. 2 as a function of kR for particles ranging in size from zero up to slightly larger than a wavelength ($kR = \pi$ corresponds to particle diameter=λ).

Even though the IA conditions can be found from the numerical solutions presented in fig. 2, absorber design will generally require taking into account the other properties of the absorber, like IA bandwidth and absorption in other modes. We illustrate this point with some plots of the dimensionless absorption cross section, $8\pi\sigma_{\rm abs}/(3\lambda^2)$, for particles designed to satisfy electric dipole IA at a few different sub-wavelength size parameters, notably $kR = 0.3$ and $kR = 1$ in fig. 3a and fig. 3b. The total absorption cross sections are plotted in blue, the electric dipole absorption cross sections in red, and as a further piece of information, the magnetic dipole absorption cross section is plotted in green.

One remarks from fig. 2 that IA can be satisfied for relatively modest values of $\Re\{\overline{\varepsilon}_s\} > 1$ for size parameters roughly larger than unity (*i.e.* $D \gtrsim \lambda/3$). For IA designed to occur at $kR = 2$, absorption cross sections are plotted for both the $\Re\{\overline{\varepsilon}_s\} < 1$ solution value of $0.4809 + i1.148$ in fig. 3c and the lowest $\Re\{\overline{\varepsilon}_s\} > 1$

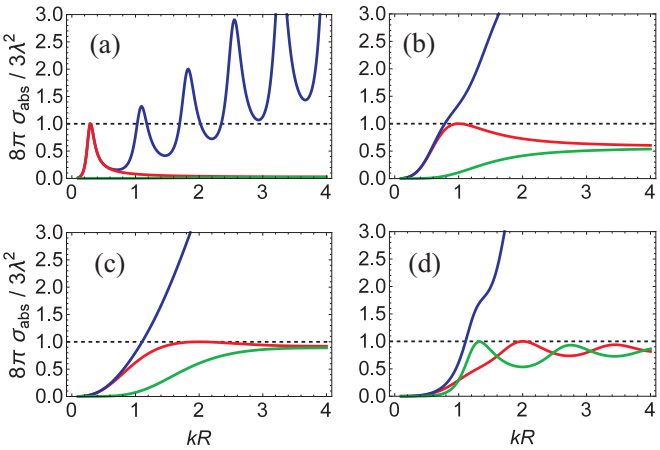

FIG. 3. Dimensionless absorption cross sections, $8\pi\sigma_{\rm abs}/(3\lambda^2)$, plotted as a function of kR for IA designed to occur at: (a) $kR = 0.3$, $\overline{\varepsilon}_s = -2.21 + i0.0611$; (b) $kR = 1$, $\overline{\varepsilon}_s = -1.87 + i2.91$; (c) $kR = 2$, $\overline{\varepsilon}_s = 0.4809 + i1.148$; and (d) $kR = 2$, $\overline{\varepsilon}_s = 4.968 + i1.361$. Total absorption cross sections are given by blue curves, electric dipole absorption by red curves, and magnetic dipole absorption by green curves.

solution of $\overline{\varepsilon}_s = 4.968 + i1.361$ in fig. 3d.

For scatterers that are quite small with respect to the IA wavelength, like $kR = 0.3$ in fig. 3a, one clearly observes peaks in the total absorption cross section associated with higher electric multi-pole modes, although only the electric dipole mode (red curve), satisfies the IA condition per its design. We remark that the magnetic dipole contributions (green curve) are insignificant at such sizes. For somewhat larger sub-λ particles, like the $kR = 1$, the electric dipole IA solution in fig. 3b, one remarks that the electric dipole IA is accompanied by non-negligible absorption in higher order modes including the magnetic dipole contribution (in green). This behavior is accentuated for $kR = 2$ with magnetic dipole contributions coming close to the IA condition in both the $\Re\{\overline{\varepsilon}_s\} < 1$ and $\Re\{\overline{\varepsilon}_s\} > 1$ designs. We remark however that even when IA occurs for both electric and magnetic dipole modes in the same particle, they cannot both be satisfied at the same frequency (for a homogeneous particle at least). We also underline the fact that for $\Re\{\varepsilon_s\} > 1$ absorbers, it can be easier to obtain magnetic dipole IA solutions than those of electric dipoles. The ability for small particles to produce strong magnetic dipole absorption at optical frequencies has also been remarked recently by other authors[35].

IV. IDEAL ABSORPTION WITH REALISTIC MATERIALS

Materials exhibiting plasmonic resonances like silver and gold are good candidates to achieve ideal absorption at small nanoparticle sizes since they provide $\Re\{\overline{\varepsilon}_s\} < 1$ and modest absorption over the visible and near visible frequencies. Even for these materials however, ideal absorption will only occur at certain frequencies and sizes, and generally requires exploiting at least one tunable parameter like the refractive index N_b of the background medium.

We plot in fig. 4a, the path traced out by $\overline{\varepsilon}_s$ for gold and silver in a water background, $N_b = 1.33$, as the vacuum wavelength of light varies from the near ultra-violet to the mid-visible range (using interpolated Johnson & Christy data[36]). The values of $\overline{\varepsilon}_s$ required for producing the lowest electric dipole IA are also plotted in this figure as the size parameter, kR, varies from 0 to 4. The values predicted for IA by the Green function point-like model are also plotted in this graph as kR varies from 0 to infinity. IA is predicted to occur at the values of kR and frequencies where the IA curves, dashed lines, intercept the experimentally determined dispersion relations, full lines.

Inspection of fig. 4a indicates 3 possible IA solutions in a water background (cf. table I), we caution that only the lowest particle sizes correspond to resonances dominated by a dipolar response. Dipole IA solutions at larger particles sizes will include significant absorption in higher order modes similar to that seen in fig. 3(c)-(d).

$D_{\rm IA}$(nm)	$\lambda_{\rm v}^{\rm (IA)}$ (nm)	$kR_{\rm IA}$	$\varepsilon_{\rm Ag}$
34.04	393.76	0.361	-4.094 + i0.199
115.53	295.80	1.63	0.704 + i3.01
291.4	321.0	3.13	0.700 + i0.856
$D_{\rm I}$ (nm)	$\lambda_{\rm v}^{\rm (IA)}$ (nm)	$kR_{\rm IA}$	$\varepsilon_{\rm Au}$
91.74	540.69	0.709	-5.30 + i2.20
121.59	451.81	1.12	-1.76 + i5.27
75.94	273.38	1.16	-1.37 + i5.17

TABLE I. Conditions to reach electric dipole IA for silver and gold nanoparticles in water medium ($N_b = 1.33$): particle diameters $D_{\rm IA}$, vacuum wavelengths $\lambda_{\rm v}^{\rm (IA)}$ and non-normalized metal permittivity ε_s.

$D_{\rm IA}$ (nm)	$\lambda_{\rm v}^{\rm (IA)}$ (nm)	$kR_{\rm IA}$	$\varepsilon_{\rm Ag}$
30.62	412.77	0.35	-5.16 + i0.227
$D_{\rm IA}$ (nm)	$\lambda_{\rm v}^{\rm (IA)}$ (nm)	$kR_{\rm IA}$	$\varepsilon_{\rm Au}$
76.23	559.68	0.64	-6.57 + i1.95

TABLE II. Conditions to reach electric dipole IA for silver and gold nanoparticles in glass medium ($N_b = 1.5$): particle diameters $D_{\rm IA}$, vacuum wavelengths $\lambda_{\rm v}^{\rm (IA)}$ and non-normalized metal permittivity ε_s.

Analogous curves are plotted in fig. 4b for a higher background index material, $N_b = 1.5$, like that typical of polymers and glass. At this higher index background medium, only one IA solution exists for both silver and gold. The IA values for gold and silver deduced from an analysis of the intercepts between the IA conditions and the experimental permittivity functions of fig. 4 are

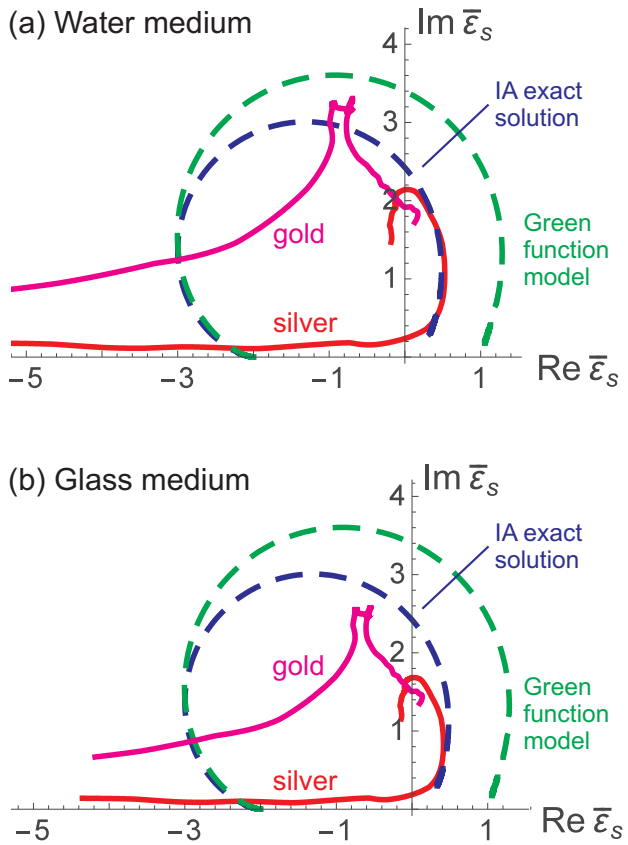

FIG. 4. Evolution of the normalized permittivity $\bar{\varepsilon}_s = \varepsilon_s/\varepsilon_b$ in the complex plane as the vacuum wavelength is varied for silver nanoparticles (red) $\lambda_v \in \{188-500\}$nm and gold nanoparticles (magenta) $\lambda_v \in \{188-600\}$nm embedded in a water medium $N_b = 1.33$ (a), and a glass medium $N_b = 1.5$ (b). The values of $\bar{\varepsilon}_s$ required to reach ideal absorption in the lowest electric dipole mode are plotted in dashed blue for kR varying from 0 to 4. The intersections between this curve and the measured metal permittivity provide the conditions to optimize absorption using silver or gold nanoparticles. Tables 1 and 2 detail these conditions for water and glass media. For comparison, we also represent the Green function point-like predictions of eq. (12) in dashed green. As already noted in Fig. 1, this model fails in accurately predicting the IA conditions.

given in table I and table II for $N_b = 1.33$ and $N_b = 1.5$ respectively.

Although IA is predicted for both silver and gold in transparent material media, one can expect significant differences in their IA behavior in view of the considerable differences in their respective dispersion relations and predicted IA sizes. This is indeed the case, as illustrated in fig. 5 where the scattering and absorption cross sections of the silver (a)-(b) and gold particles (c)-(d) are plotted for frequencies in the visible range for particles whose IA diameters are taken from table II ($D_{\rm IA} = 30.6$nm ($\lambda_v = 413$nm) for silver and $D_{\rm IA} = 76.2$nm $\lambda_v = 560$nm for gold).

The frequencies at which IA is predicted are indicated by vertical dashed lines, and the IA cross sections of $8\pi\sigma_{\rm abs}/(3\lambda^2) = 1$ are indicated by horizontal dashed lines in these figures. The total absorption and scattering cross sections are drawn in blue, and electric dipole contributions are drawn in red, but these curves are nearly indistinguishable on the scale of these graphs except for short wavelengths in gold. Magnetic dipole contributions are plotted in green, but are negligible in all graphs excepting some mild magnetic dipole absorption in gold at short wavelengths.

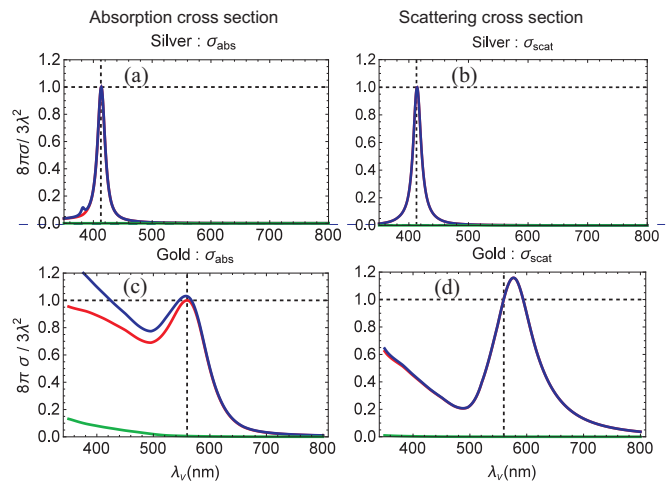

FIG. 5. Absorption (a) and scattering (b) cross sections for silver nanoparticles designed to reach IA in glass medium $N_b = 1.5$ (blue curves). Dipole contributions to the cross sections are plotted in red for the electric dipole and green for the magnetic dipole. The silver nanoparticle diameter is $D_{\rm IA} = 30.6$nm. The IA wavelength is specified by a vertical dashed line, and corresponds to the situation of the cross section reaching the limit of eq. (6). (c,d) Same as (a,b) for gold nanoparticles of diameter $D_{\rm IA} = 76.2$nm.

In fig. 5, one remarks significant differences between the respective behaviors of silver and gold IA particles near their IA resonances. Notably, the electric quadrupole, magnetic dipole and higher order corrections are essentially negligible near the silver IA resonance, while non-electric dipole orders contribute significantly to absorption (but not scattering) at wavelengths below the IA resonance in gold. One should also remark that although the dipole contributions to the absorption cross sections are limited by their theoretical upper bound of $\sigma_{\rm abs} = 3\lambda^2/(8\pi)$, the electric dipole scattering cross section of gold rises to values above $3\lambda^2/(8\pi)$, at frequencies below the IA resonance, but this is allowed by the general theoretical considerations of eq. (5) where one sees that the scattering cross section of a dipole mode is only required by unitarity to satisfy $\sigma_{\rm scat} \leq 3\lambda^2/(2\pi)$. Nevertheless, one can see in both fig. 5b and fig. 5d that $\sigma_{\rm scat} = 3\lambda^2/(8\pi)$ at the IA resonance as required by the general theoretical restraint of eq. (6).

V. IDEAL ABSORPTION FOR CORE-SHELL NANOPARTICLES

Although we saw that changing the background material index allows some control over IA frequency with homogeneous inclusions, applications are likely to request IA to occur at particular frequencies with a set of available materials. This requires additional adjustable geometric parameters and concentric coatings is one of the simplest ways to achieve this.

If we consider inclusions consisting of a core and a single concentric coating, one has two adjustable parameters, the radius of the outer shell R, and its concentric spherical core, R_c (cf. fig. 6). It proves convenient to fix these two dimensioned parameters, R and R_c, in terms of the dimensionless size parameter, kR, and core material filling factor $f \equiv (R_c/R)^3$. Unlike the homogeneous sphere studied in the previous section, the analytic properties of the S matrix cannot be directly exploited to determine the parameters producing IA solutions, since no IA solutions are guaranteed to exist when varying the parameters kR and f of a coated sphere with fixed permittivities.

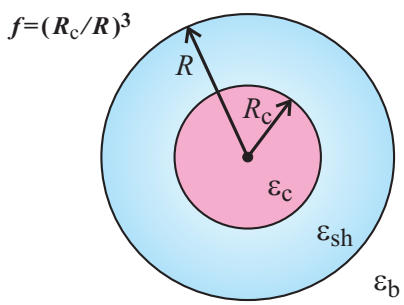

FIG. 6. Schematic of a concentric coated sphere where the core, shell, and background permittivities are denoted respectively ε_c, ε_{sh}, and ε_b. The filling fraction of the core material is defined as $f \equiv (R_c/R)^3$.

Given the complexity of the analytic coated sphere solutions, the possible non-existence of solutions at finite frequency, and finally the fact that there are multiple adjustable parameters, it is advantageous to develop compact approximate formulas that allow one to rapidly determine which parameters and materials can provide viable designs for coated sphere ideal absorbers. We derive now an approximation which allows the design of core-shell electric dipole IA scatterers by taking advantage of the fact that one is generally interested in designing sub-wavelength IA particles.

We saw that eq. (16a) provides an accurate approximation for the required IA permittivity contrast, $\overline{\varepsilon}_s$, over the entire range of the size parameter $\rho = kR$. The Maxwell-Garnett effective medium approach is derived as the effective permittivity of a concentric sub-wavelength core-shell particle whose volume fraction matches that of the bulk material. The effective permittivity, $\overline{\varepsilon}_{\rm eff}$, of a core-shell system can thus be written as a function of filling fraction, f:[37]

$$\overline{\varepsilon}_{\rm eff} = \overline{\varepsilon}_{\rm sh}\left(1 + 3f\frac{\overline{\varepsilon}_{\rm c} - \overline{\varepsilon}_{\rm sh}}{\overline{\varepsilon}_{\rm c} + 2\overline{\varepsilon}_{\rm sh} - f(\overline{\varepsilon}_{\rm c} - \overline{\varepsilon}_{\rm sh})}\right) . \qquad (17)$$

where $\overline{\varepsilon}_{\rm sh}$ and $\overline{\varepsilon}_{\rm c}$ are the shell and core relative permittivities respectively. This equation can then be algebraically inverted to yield filling fraction as a function of $\overline{\varepsilon}_{\rm eff}$ *i.e.*:

$$f = \frac{\varepsilon_c + 2\varepsilon_{\rm sh}}{\varepsilon_c - \varepsilon_{\rm sh}}\frac{\varepsilon_{\rm eff} - \varepsilon_{\rm sh}}{\varepsilon_{\rm eff} + 2\varepsilon_{\rm sh}} \qquad (18)$$

One can then solve for core-shell IA by replacing the "effective" index in eq. (18) by the $\overline{\varepsilon}^{(e)}$ of eq. (16a) that specifies the permittivity required for the IA condition. Since $\overline{\varepsilon}_{\rm eff}$ and at least one of the materials is complex valued, the filling fraction, f, found by eq. (18) is generally complex, but one can vary the size parameter, $\rho = kR$ to obtain a $\Im\{f\} = 0$ solution graphically. Provided that the real part of the filling fraction is less than 1 when $\Im\{f\} = 0$, then one has found a valid IA solution.

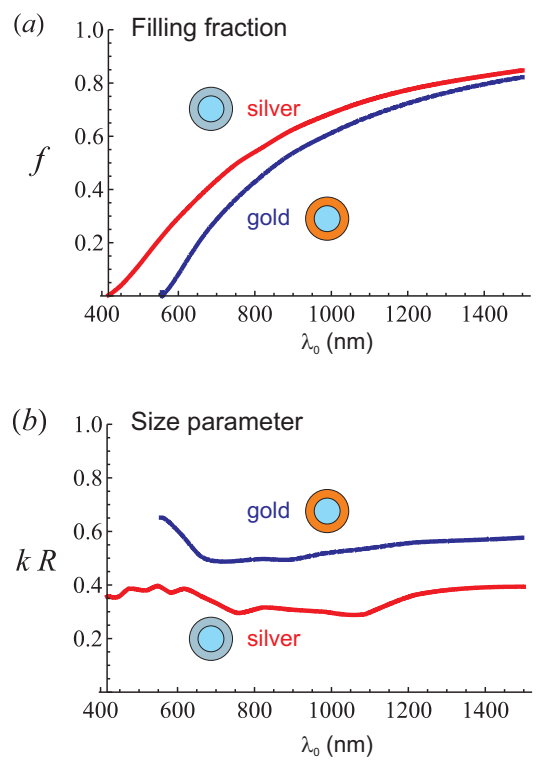

FIG. 7. Plots of the filling fraction (a) and the size parameter (b), required to achieve IA in a core shell structure immersed in a $N_b = 1.5$ background material. The core is considered to be a lossless high index material, $N_c = 2.8$, and the shell is either silver (red solid line) or gold (blue dashed line).

We apply the graphic solution method described in the previous paragraph to the core-shell IA design consisting of a silver or gold metallic layer around a lossless high index core of $N_c = 2.8$ in a background medium of index $N_b = 1.5$. The results are illustrated in fig. 7. The filling fractions of the shell material and the radius of

the particle are given as a function of the vacuum wavelength of the incident field. We remark that the chosen core-shell design with a high index center and a metallic shell allows one to design IA for any wavelength higher than the homogeneous sphere solutions given in table II. It is also possible to design IA for other geometries, like a dielectric shell around a metallic core, but the metallic shell design illustrated here tended to give the smallest IA solutions and seemed more realizable from a practical standpoint.

VI. CONCLUSIONS

In this work, we have derived simple analytical expressions, Eqs.(16), to accurately predict the lowest order electric and magnetic modes leading to Ideal Absorption (IA). These expressions provide a significant improvement as compared to the classical 'point-like' models derived using Green's function or Mie coefficients expansion, and can accurately handle nanoparticle sizes up to several wavelengths. The IA criteria was shown to correspond to a limit behavior of an absorption cross section channel. Precise electromagnetic calculations in the complex frequency plane were also introduced to predict this phenomenon, indicating the intriguing possibility of observing IA in high index absorbing materials and not just in metals. Our results showed that IA should be observable at visible frequencies for homogeneous nanoparticles composed of gold or silver for specific (fixed) frequencies and sizes. The methods and formulas developed in this work led to a simple scheme (eq. (18)) for predicting core-shell geometries supporting effective IA conditions throughout the visible spectrum. Experimental observations of IA for optimized sub-wavelength particles are within reach and should prove useful to better understand IA and its signature in quantum systems.

The authors would like to thank Guillaume Baffou and Xavier Zambrana for interesting discussions and helpful remarks. The research leading to these results has received funding from the European Research Council under the European Union's Seventh Framework Programme (FP7/2007-2013) / ERC Grant agreements 278242 (ExtendFRET), and from the A*MIDEX project (n° ANR-11-IDEX-0001-02) funded by the Investissements d'Avenir French Government program managed by the French National Research Agency (ANR).

[1] S.Lal, S.Link, N.Halas, Nano-optics from sensing to waveguiding, J. Nat. Photonics 2007, **1**, 64–648 (2007).
[2] J.A.Schuller, E.S.Barnard, W.S.Cai, Y. C.Jun, J. S.White, M. L.Brongersma, Plasmonics for extreme light concentration and manipulation, Nat. Mater., **9**, 193–204 (2010).
[3] L.Novotny, N.van Hulst, Antennas for light, Nat. Photonics, **5**, 83–90 (2011).
[4] H. A.Atwater, A.Polman, Plasmonics for improved photovoltaic devices, Nat. Mater., **9**, 205–213 (2010).
[5] G. Baffou, R. Quidant, Thermo-plasmonics: using metallic nanostructures as nano-sources of heat. Laser & Photonics Reviews, **7**, 171-187 (2013).
[6] K.M.Mayer, J. H.Hafer, Localized surface plasmon resonance sensors, Chem. Rev., **111**, 3828–3857 (2011).
[7] N. J.Halas, S.Lal, W.S.Chang, S.Link, P.Nordlander, Plasmons in strongly coupled metallic nanostructures, Chem. Rev., **111**, 3913–3961 (2011).
[8] G. Baffou, R. Quidant, Nanoplasmonics for Chemistry. Chem. Soc. Rev. **43**, 3898 (2014).
[9] Y. D. Chong, Li Ge, and Hui Cao, and A.D. Stone, Coherent Perfect Absorbers: Time-Reversed Lasers, Phys. Rev. Lett., **105**, 053901 (2010).
[10] H. Noh, Y. Chong, A. D. Stone, and H. Cao, Perfect coupling of light to surface plasmons by coherent absorption, Phys. Rev. Lett., **108**, 186805 (2012)
[11] H. Noh, S.M. Popoff, and H. Cao, Broadband subwavelength focusing of light using a passive sink, Optics Express, **21**, 17435-17446 (2013)
[12] A. Sentenac, P. C. Chaumet, and G. Leuchs, Total absorption of light by a nanoparticle: an electromagnetic sink in the optical regime, Opt. Lett., **38**, 818–820, (2013).
[13] V. Grigoriev, A. Tahri, S. Varault, B. Rolly, B. Stout, J. Wenger, N. Bonod, Optimization of resonant effects in nanostructures via Weierstrass factorization, Phys Rev. A, **88**, 011803 (2013).
[14] V. Grigoriev, S. Varault, G. Boudarham, B. Stout, J. Wenger, N. Bonod, Singular analysis of Fano resonances in plasmonic nanostructures, Phys Rev. A, **88**, 063805 (2013).
[15] L. Tsang, J. A. Kong, K.-H. Ding, *Scattering of Electromagnetic Waves*, Vol.1, Wiley series in Remote sensing, John Wiley & Sons New York, (2000).
[16] B. Stout, J.C. Auger, A. Devilez, Recursive T matrix algorithm for resonant multiple scattering: Applications to localized plasmon excitations, J. Opt. Soc. Am. A, **25**, 2549-2557 (2008).
[17] R.G. Newton, *Scattering Theory of Waves and Particles*, McGraw-Hill New York, (1966).
[18] H.C. van de Hulst, *Light scattering by small particles*, Dover Publications, (1957).
[19] C. F. Bohren and D. R. Huffman, *Absorption and Scattering of Light by Small Particles*, Wiley-Interscience, New York (1983).
[20] R. Fleury, and J. Soric, and A. Alù, Physical bounds on absorption and scattering for cloaked sensors, Phys. Rev. B, **89**, 045122(12), (2014).
[21] S. Tretyakov, Maximizing Absorption and Scattering by Dipole Particles, Plasmonics, **9**, 935-944, (2014)
[22] T.A. Nieminen, H. Rubinsztein-Dunlop, and N.R. Heckenberg, Calculation of the T-matrix: General considerations and application of the point-matching method, J. Quant. Spect. & Rad. Trans. **79-80**, 1019-1029 (2003).
[23] L.C. Botten, R.C. McPhedran, N.A. Nicorovici, and G.H. Derrick, Periodic Models for Thin Optimal Ab-

sorbers of Electromagnetic Radiation, Phys. Rev. B (Rapid Comm.), **55**, R16072-R16075, (1997).

[24] A. K. Sarychev, D. J. Bergman, and Y. Yagil, Theory of the optical and microwave properties of metal-dielectric films, Phys. Rev. B, American Physical Society, **51**, 5366-5385 (1995).

[25] P. de Vries, D.V. van Coevorden, A. Lagendijk, Point scatterers for classical waves, Rev. Mod. Phys, **70**, 447-466, (1998).

[26] Y.-P. Pellegrini, P. Thibaudeau, B. Stout, Off-shell mean-field electromagnetic T-matrix of finite size spheres and fuzzy scatterers, J. Phys. Condens. matter, **9**, 177-191 (1997).

[27] A. Moroz, Depolarization field of spheroidal particles, J. Opt. Soc. Am. B **26**, 517-527 (2009).

[28] E.C. Le Ru, W.R.C. Somerville, and B. Auguié, Radiative correction in approximate treatments of electromagnetic scattering by point and body scatterers Phys. Rev. A **87**, 012504 (2013).

[29] S. Albaladejo , R. Gómez-Medina, L. S. Froufe-Pérez, H. Marinchio, R.Carminati, J. F. Torrado, G. Armelles, A. Garcia-Martin, and J.J. Sáenz, Radiative corrections to the polarizability tensor of an electrically small anisotropic dielectric particle, Opt. Exp. **70**, 3563 (2010).

[30] G.Colas des Francs, C. Girard, A. Bruyant, and A. Dereux, SNOM signal near plasmonic nanostructures: An analogy with fluorescence decay channels, J. of Micr., **229**, 302-306 (2007).

[31] G.Colas des Francs, A. Bouhelier, E. Finot, J.C. Weeber, A. Dereux, C. Girard, E. Dujardin, Fluorescence relaxation in the near–field of a mesoscopic metallic particle: distance dependence and role of plasmon modes, Opt. Express, **16**, 17654-17666 (2008).

[32] J.A. Stratton, *Electromagnetic Theory*, Wiley, IEEE Press reissue 2007 (1947).

[33] B. Stout, A. Devilez, B. Rolly, N. Bonod, Multipole methods for nanoantennas design: applications to Yagi-Uda configurations, J. Opt. Soc. Am. B, **28**, 1213-1223 (2011).

[34] G.N. Watson, Cambridge University Press, Cambridge, *A Treatise on the Theory of Bessel Functions*, Cambridge University Press, Cambridge (1980).

[35] A. Asenjo-Garcia, A. Manjavacas, and V. Myroshnychenko and F.J. García de Abajo, Magnetic polarization in the optical absorption of metallic nanoparticles, Opt. Express, **20**, 28142-28152 (2012).

[36] P. B. Johnson and R.W. Christy, Optical Constants of the Noble Metals, Phys. Rev. B, **6**, 4370-4379 (1972).

[37] Tuck Choy, *Effective Medium Theory (1st ed.)*, Oxford: Oxford University Press. **20**, ISBN 978-0-19-851892-1 (1999).